Upper limit for the effect of elastic bending stress on the saturation magnetization of La_{0.8}Sr_{0.2}MnO_{3}

Q. Wang, A. P. Chen, E. J. Guo, M. A. Roldan, Q. X. Jia, and M. R. Fitzsimmons

1 **The upper limit of effect of elastic bending stress on the saturation magnetization of**

2 **$La_{0.8}Sr_{0.2}MnO_3$**

3

4 Q. Wang,[1,2] A. P. Chen,[3] E. J. Guo,[4] M. A. Roldan,[5] Q. X. Jia,[3,6] M. R. Fitzsimmons[4,7]

5 [1]Materials Science Division, Argonne National Laboratory, Argonne, IL 60439, USA

6 [2]Department of Physics and Astronomy, West Virginia University, Morgantown, West Virginia 26506,

7 USA

8 [3]Center for Integrated Nanotechnology, Los Alamos National Laboratory, Los Alamos, NM 87545, USA

9 [4]Neutron Scattering Division, Oak Ridge National Laboratory, Oak Ridge, TN 37831, USA

10 [5]Imaging and Characterization Core Lab, King Abdullah University of Science and Technology (KAUST),

11 Thuwal 23955-6900, Saudi Arabia

12 [6]Department of Materials Design and Innovation, University at Buffalo, The State University of New York,

13 Buffalo, NY 14260, USA

14 [7]Department of Physics and Astronomy, University of Tennessee, Knoxville, TN 37996, USA

15

16 Using polarized neutron reflectometry (PNR), we measured the influence of

17 elastic bending stress on the magnetization depth profile of a $La_{0.8}Sr_{0.2}MnO_3$ (LSMO)

18 epitaxial film grown on a $SrTiO_3$ (STO) substrate. The elastic bending strain of $\pm 0.03\%$

19 has no obvious effect on the magnetization depth profile at saturation. This result is in

20 stark contrast to that of $(La_{1-x}Pr_x)_{1-y}Ca_yMnO_3$ (LPCMO) films for which strain of $\pm$

21 0.01% produced dramatic changes in the magnetization profile and Curie temperature.

22 We attribute the difference between the influence of strain on the saturation

23 magnetization in LSMO (weak or none) and LPCMO (strong) to a difference in the

24 ability of LSMO (weak or none) and LPCMO (strong) to phase separate. Our observation

25 provides an upper limit of tuning LSMO saturation magnetization via elastic strain effect.

Introduction

Numerous efforts have been made to find magnetoelectric multiferroic (MF) materials that exhibit strong coupling between ferromagnetic (FM) and ferroelectric (FE) order parameters[1,2,3] at room temperature. Such functionality provides intriguing opportunities for next-generation data storage, sensor, and actuator technologies.[4] Coupling of FM and FE order parameters is rare in single phase materials.[5] Exceptions often exhibit weak magnetoelectric coupling at low temperatures. As an alternative to single phase materials, nanocomposites of FM and FE materials show promise. The doped-manganite perovskites, e.g., $La_{1-x}Sr_xMnO_3$ (LSMO), have been chosen as one of the best FM materials in MF nanocomposites fabrication due to their superior magnetic properties and the versatile phases at different doping across the phase diagram.[6] Diverse types of LSMO/FE heterostructure, such as $LSMO/BaTiO_3$ (BTO),[7] $LSMO/[Pb(Mg_{1/3}Nb_{2/3})O_3]_{1-x}[PbTiO_3]_x$ (PMN-PT),[8,9] and $LSMO/Pb(Zr_{0.2}Ti_{0.8})O_3$ (PZT),[10,11] have been grown and extensively studied to realize the magnetoelectric couplings and different mechanisms have been proposed. Changes of ordering temperature and (near) remanent magnetization of LSMO films have been documented in LSMO/BTO heterostructures during BTO phase transformation[7] and in LSMO/PMN-PT heterostructures as responding to the external electric field,[8,9] and have been attributed to the strain effects. More recently, the magnetic properties of LSMO films were observed to be affected by proximity to PZT and have been attributed to hole accumulation or depletion at LSMO/PZT interface caused by the change of PZT polarization under different electric field rather than strain.[10,11]

48   In general, the change of polarization in FE materials is always associated with

49   crystal distortion. Thus in LSMO/FE heterostructures, one should not exclude strain as a

50   contributing factor influencing the interfaced LSMO magnetic properties when applying

51   electric field across FE. In order to distinguish between these two mechanisms, we

52   examined the influence of applied elastic bending stress on the magnetization of

53    $La_{0.8}Sr_{0.2}MnO_3$ epitaxial films grown on $SrTiO_3$ (STO) using polarized neutron

54   reflectometry (PNR) technique with a four-point bending jig.[12,13] This allowed us to

55   investigate the exclusive role of strain on the LSMO magnetization properties. We found

56   that elastic bending strain of $\pm 0.03\%$ has no obvious effect on the magnetization depth

57   profile at saturation. This result is in stark contrast to that of $(La_{1-x}Pr_x)_{1-y}Ca_yMnO_3$ (x ~

58   0.60, y ~ 0.20 and 0.33) (LPCMO) films for which strain of $\pm 0.01\%$ produced dramatic

59   changes in the magnetization profile and Curie temperature.[12,13] We further attribute the

60   difference between the influence of strain on the saturation magnetization in LSMO

61   (weak or none) and LPCMO (strong) to a difference in the ability of LSMO (weak or

62   none) and LPCMO (strong) to phase separate. Our observation provided an upper limit of

63   tuning LSMO saturation magnetization using strain effect and also shed new light on

64   designing functional spintronic devices using strain/charge effect across manganites/FE

65   interfaces. Namely, that strain may be less of a factor influencing magnetism in a

66   manganite/FE heterostructure than other factors, e.g., charge doping.

67   **Sample preparation and chemical characterization**

68   High quality epitaxial LSMO (x = 0.2) films (47 nm) were grown on 1 cm × 1 cm

69   STO (001) substrates (250 μm thick) by pulsed laser deposition (PLD, KrF excimer laser,

70   λ=248 nm). The substrate temperature was maintained at 750 °C. A low oxygen pressure

71 of 50 mTorr and low laser repetition rate were used to grow high quality thin films with

72 smooth surfaces.[14] The rectangular laser beam with an area of 5.55 mm^2 was focused

73 onto the target with an energy density of 2 J/cm^2. An image beam method was used to

74 obtain stabilized and uniform laser energy density on the target.[15] After deposition, films

75 were annealed *in situ* at 600 °C and 500 Torr oxygen for 30 minutes before cooling to

76 room temperature at 5 °C/min. The orientation, thickness and original strain states of

77 films were investigated by high resolution X-ray diffraction (XRD) using PANalytical

78 MRD PRO X-ray diffractometer with the Triple Axis option, as shown in Figures 1(a)

79 and 1(b). The XRD measurements indicated that the LSMO film was epitaxially grown

80 on the STO substrate.

81   The chemical density profile, including film thickness and roughness was

82 obtained from X-ray reflectometry (XRR). The XRR normalized to the asymptotic value

83 of the Fresnel reflectivity ($R_F = 16\pi^2/Q^4$) is plotted in Figure 1(c) versus wave vector

84 transfer Q ($= 4\pi \times \sin\theta / \lambda$). θ is the angle of incidence between the incident wave vector

85 and its projection onto the sample's surface; λ is wavelength. Calculated reflectivities

86 were obtained from a model representing the LSMO film with a bulk region and a very

87 thin (~ 1 nm) surface region on STO using the Parratt formalism.[16,17] The model was

88 refined to optimize a goodness-of-fit.[18,19] The x-ray scattering length density (SLD)

89 profiles of the model are shown in the inset of Figure 1(c). The model provides values of

90 the surface and interface roughness and layer thicknesses used to constrain the analysis of

91 the PNR data presented later. The existence of the thin surface layer with slightly reduced

92 X-ray SLD could be due to the surface contamination or degradation of the LSMO films

93 at the LSMO/air interface.

94   Scanning transmission electron microscopy (STEM) and electron energy-loss

95   spectroscopy (EELS) measurements were performed on a thinner (34 nm) LSMO/STO

96   sample, which was grown using the same system and under the same growth conditions.

97   Consistent with the XRD and XRR studies discussed above, The STEM result (Figure

98   1(d)) indicates excellent epitaxial growth. No noticeable variation of the lattice spacing of

99   LSMO either parallel or perpendicular to the LSMO/STO interface was detected by

100   Fourier analysis of the TEM images, *i.e.,* no evidence for non-uniformity of strain in the

101   film was observed. The EELS imaging indicates the chemical composition of the film

102   bulk to be exceedingly uniform (Figure 1(e)). The chemistry of the surface is more

103   ambiguous due to electron beam broadening effects resulting from dechanneling.

104   **Magnetometry and magnetotransport measurements**

105   The temperature and field dependence of the magnetization of the 47 nm LSMO

106   films were measured by a superconducting quantum interference device (SQUID)

107   magnetometer. The magnetic field was applied parallel to the film plane. At 50 K, the

108   magnetization in the plane of the sample, M, taken as a function of field, H, is shown in

109   Figure 2(a), inset. The magnetization was recorded after cooling in a field of 5 kOe as

110   shown in Figure 2(a), from which a Curie temperature of 317 K was obtained.

111   For magnetotransport measurements, Au electrodes were patterned on bar shaped

112   thin films (2 mm × 10 mm). The resistance of LSMO films was measured by standard

113   four-probe method using a physical property measurement system (PPMS). As shown in

114   Figure 2(b), measurements were made under different magnetic field ($\mu_0 H$ = 0, 1, 5, and

115   7 T) applied perpendicular to the film plane and for warming and/or cooling cycles. The

116   current was measured across the surface of the film. The heating/cooling rate during data

117 collection was 2 K/min, and the sample had been thermally demagnetized before the

118 measurements. The magnetotransport curves show the magnetoresistance effect and

119 metal-insulator transition (MIT) with $T_c \sim 315$ K at zero field and increasing with

120 magnetic fields. Furthermore, under 0 T and 1 T field no hysteresis behavior was

121 observed in the transport during cooling/warming cycles, thus, we see no evidence for

122 phase separation which usually gives rise to hysteresis as was the case for LPCMO thin

123 films.[12,13] Here we also note that for the magnetoresistance measurement, the direction of

124 the applied field is perpendicular to the film instead of within the film, which is

125 determined by the available experimental setup of the instrument. Though the missing of

126 the resistance hysteresis is a universal behavior and independent to the applied field

127 direction.[20]

128 **PNR study on bending sample**

129   Bending stress was applied to the 47 nm LSMO film using a four-point bending

130 jig in the method described in Ref. 1. Depending upon the orientation of the film with

131 respect to the jaws of the bending jig, compressive or tensile bending stress can be

132 applied, as indicated in the insets of Figures 3(a) and 3(c). The radius of curvature of the

133 sample was oriented normal to the scattering plane of the neutron experiment so that the

134 bent sample did not affect the width of the specularly reflected neutron beam. The PNR

135 result (Figures 3(a)-3(c)) was obtained using the Asterix spectrometer at the Los Alamos

136 Neutron Science Center.[21] The sample was cooled to 10 K in a field of H = 5 kOe and

137 measured in this field. The reflectivities were measured for bending strains of $\varepsilon =$

138 $- 0.03\%$ (compression), $\varepsilon = 0$ and $\varepsilon = +0.03\%$ (tension). The bending strain of the film

139 was measured using[22] $\varepsilon = t_s/R$, where t_s and R are the thickness of substrate and the radius

140   of the curvature of the film, respectively. The radius of curvature of the sample was

141   measured with a laser.[23]

142   The specular reflectivity, R, is determined by the neutron scattering length density

143   (SLD) depth profile, $\rho(z)$, averaged over the lateral dimensions of the sample.

144     $\rho(z)$ consists of nuclear and magnetic SLDs such that $\rho^{\pm}(z) = \rho_n(z) \pm CM(z)$, where C

145     $= 2.91 \times 10^{-9}\,\text{Å}^{-2}\,(\text{kA/m})^{-1}$ and $M(z)$ is the magnetization (a moment density obtained in

146   kA/m) depth profile.[21] The +(-) sign denotes neutron beam polarization parallel

147   (opposite) to the applied field and corresponds to reflectivities, $R^{\pm}(Q)$. Thus, by

148   measuring $R^+(Q)$ and $R^-(Q)$, $\rho_n(z)$ and $M(z)$ can be obtained separately. The nuclear

149   SLD and magnetization depth profiles are shown in Figures 3(d) and 3(e). Consistent

150   with the XRD, STEM, and EELS studies, the nuclear SLD exhibits uniform chemical

151   composition throughout the film. Compared with the XRR result which suggested

152   slightly reduced X-ray SLD within the surface region, the obtained magnetization depth

153   profile does suggest reduced magnetization (region I in Figure 3(d)) at the LSMO surface

154   for all strain cases. The reduction could be due to a perturbed electron

155   configuration/distribution at the surface (indicated by the Xray SLD) and/or be sensitive

156   to the surface termination. PNR fits also indicate reduced magnetization at the

157   LSMO/STO interface. This is consistent with neutron scattering experiments of films and

158   superlattices of other groups, which also report a magnetically degraded interface

159   region.[12,24] Magnetic depletion layers at interfaces have been attributed to change of

160   chemistry[12] (though our data indicate this is not the case for our samples), strain, or

161   discontinuity of interface charge. In the present study, our sample is close to uniformly

162   strained (evidence from TEM) in the absence of bending stress. In the bending case, the

163   magnitude of the variation of the applied bending strain across the thickness of the film is

164   very small; approximately 4×10^{-4} times the bending strain. We note the charge

165   discontinuity across the LSMO/STO interface is 0.8 e$^-$ per lateral unit cell. It is often

166   cited that the charge discontinuity at the interface might cause the depletion layer,[24]

167   though Guo *et al.* recently reported that the charge discontinuity could enhance the

168   magnetization instead.[25]

169   **Bending effect on LSMO magnetization**

170   Returning to the question of what is the influence of elastic bending stress on

171   magnetism of LSMO, suppose the magnetization and elastic strain are coupled in LSMO,

172   the total magnetization on application of strain is then given by $M^2 = M_0^2 + M_\epsilon^2 = M_0^2 -$

173    $(Y/\gamma) \times \varepsilon$, where Y is Young's modulus and γ is the magnetoelastic coefficient.[12] In

174   Figure 4, we show M^2 vs. ε curves for LSMO bulk and interfacial regions obtained from

175   PNR and fit both with a linear function. Very similar slopes for both lines, $-Y/\gamma = (0.2 \pm$

176    $0.1) \times 10^8$ $(kA/m)^2$, are obtained. Previously, we examined the role of elastic bending

177   stress on the saturation magnetization and ordering temperature of LPCMO epitaxial

178   films using the same technique.[12,13] Specifically, bending stress yielding very small ~

179   0.01% compressive strain greatly increased the magnetization by ~ 20% and the Curie

180   temperature by ~ 5% compared to the case for no applied stress. Applied tensile bending

181   stress of the same magnitude decreased the magnetization and Curie temperature by

182   similar amounts. In Figure 4, we also plot the M^2 vs. ε results obtained from LPCMO

183   sample for direct comparison. For the LPCMO bulk region, $-Y/\gamma = - (8 \pm 1) \times 10^8$

184    $(kA/m)^2$ near the MIT transition temperature T_c (78 K) and $-Y/\gamma = - (6 \pm 1) \times 10^8$

185    $(kA/m)^2$ at a temperature way well below T_c (20 K) were obtained. Compared to

186   LPCMO, the saturation magnetization in LSMO has very weak or negligible response to

187   the elastic bending stress for $\varepsilon = \pm 0.03\%$.

188   Our magnetotransport measurements on LSMO films show no hysteresis behavior

189   during cooling and warming cycles, in stark contrast to LPCMO films which present a ~

190   20 K difference in MIT transition temperature between cooling and warming cycles and

191   suggest the existence of phase separation and competition. The influence of bending

192   stress on the Curie temperature of LPCMO greatly exceeds theoretical predictions for the

193   case of biaxial strain in $La_{1-x}Sr_xMnO_3$ (LSMO).[26] On the other hand, some theoretical

194   work attributes phase co-existence (or phase separation, phase texture, *etc.*) to a complex

195   landscape consisting of non-linear relationships between strain and rearrangement of the

196   unit cell contents,[27] which suggests LPCMO could be sensitive to stress.[28,29] Thus we

197   conclude from this result that bending stress has a very weak to negligible effect on a

198   system that shows weak or no phase separation (LSMO) compared to one that can be

199   strongly phase separated (LPCMO). This result reinforces the hypothesis that the strain-

200   energy landscape is a crucial factor determining the magnetic properties of materials that

201   phase-separated.

202   Previously, Lee *et al.*[7] measured the (near) remanent magnetization of 50 nm

203   thick $La_{0.67}Sr_{0.33}MnO_3$ films grown on $BaTiO_3$ (001) substrates. The data were collected

204   as a function of temperature to measure the influence of stress imposed on the film due to

205   the tetragonal (*T*) to monoclinic (*M*) and monoclinic to rhombohedral (*R*) phase

206   transformations. They defined the term $\varepsilon_a = 1/2(\varepsilon_{xx} + \varepsilon_{yy})$ which is a measure of the in-

207   plane change of area occurring due to a structural phase transformation of the substrate.

208   A positive value of ε_a results from an expansion or tensile stress. They reported changes

209   of magnetization to be $\sim$ 250% and 12% for T to M (ε_a = +0.21%) and M to R (ε_a =

210   +0.10%), respectively. Furthermore, Lee *et al.*[7] reported an *expansion*, + ε_a, is

211   accompanied by an *increase* of remanent magnetization. This enhancement, below Curie

212   temperature, is mainly attributed to the reversal of magnetic anisotropy due to the

213   structural phase transformation.

214   Subsequently, Thiele *et al.*[8,9] measured the influence of biaxial strain on the (near)

215   remanent magnetization of 20 to 50 nm thick $La_{0.7}Sr_{0.3}MnO_3$ thin films grown on PMN-

216   PT (001) FE single crystal substrates. For the case of biaxial strain ε_{xx} = ε_{yy}, ε_a can be

217   obtained. Using data shown in Figure 5 of Ref. 9, a change of ε_a = +0.15% produced

218   a change of -25% in the remanent magnetization at 330K but no detectable strain effect

219   on the remanent magnetization at low temperatures. Note, Thiele *et al.*[8,9] report

220   *expansion* in-plane strain, + ε_a, is accompanied by a *decrease* of remanent magnetization.

221   For the case of bending plate strain as realized in our experiment, ε_{yy} = 0, so ε_a =

222    $0.5 \times (\pm 0.03\%) = \pm 0.015\%$.[30] (The bending jig enables measurement of magnetism in

223   response to both tensile and compressive strain.) With strain of order $|\varepsilon_a|$ = 0.015%, no

224   statistically significant change of the LSMO saturation magnetization was observed. The

225   important distinction between our work and the previous studies is that we have

226   measured the influence of stress on the saturation magnetization, while previous work has

227   measured the (near) remanent magnetization. Thus, our experiment is not affected by

228   changes of anisotropy induced by strain. The previous studies used BTO and PMN-PT

229   substrates, both FE's, which could potentially alter the charge of the LSMO/FE interface.

230   In our experiment, we only applied mechanical stress across the sample. The different

231   observations of the studies of Lee *et al.*[7] and Thiele *et al.*[8,9] might be reconciled by

232   considering both the influence of strain on anisotropy at remanent and the interfacial

233   polarization effect from BTO and PMN-PT, which requires further investigation.

234   The bending strain applied in our experiment is fully elastic. Considering that the

235   Young's modulus of manganites is in the order of 200 GPa[31] and the yield strength of

236   perovskite ceramic (e.g., $SrTiO_3$) is in the order of 120 to 300 MPa,[32] the upper limit of

237   elastic strain of a manganite film is in the order of 0.06% to 0.15%. If we choose 0.15%

238   as the upper limit of elastic strain and assume the linear relation between M^2 and ε

239   persists within the full range, the maximum change of the saturation magnetization of

240   LSMO due to the elastic strain effect is less than 10%. To further test our result and to

241   even explore the influence of the inelastic strain on the LSMO film's magnetization,

242   additional experiments are needed which could achieve higher strain without introducing

243   extra degree of freedom, e.g., using pressure cell for PNR experiment.

244   **Conclusions**

245   In conclusion, we have measured the magnetization depth profile across a LSMO

246   (x = 0.2) epitaxial film epitaxially grown on (001) STO. The neutron measurements were

247   performed as a function of applied elastic bending stress. With bending strain $\varepsilon =$

248    $\pm$ 0.03%, no obvious influence of strain on the LSMO saturation magnetization depth

249   profile was observed, this is very different from the previously studied LPCMO films.

250   We attribute the difference between the influence of strain on the saturation

251   magnetization in LSMO (weak or none) and LPCMO (strong) to a difference in the

252   tendency of LSMO (weak or none) and LPCMO (strong) to phase separate. The upper

253   limit of tuning LSMO saturation magnetization using elastic strain is also discussed.

254   **Acknowledgements**

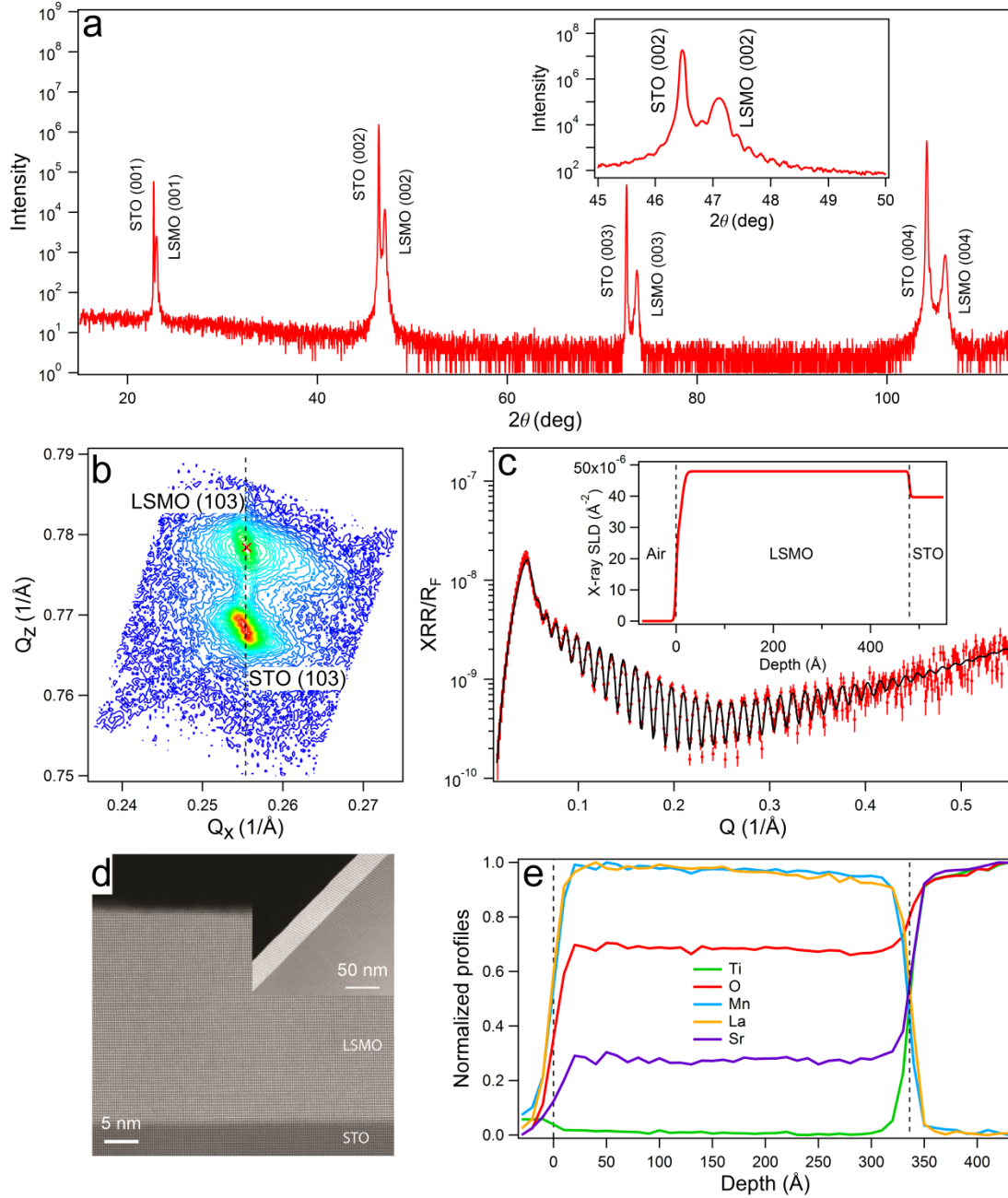Figure 1. (a) X-ray diffraction θ/2θ scan for LSMO/STO film. Inset: θ/2θ scan around STO (002) and LSMO (002) peaks. (b) Reciprocal space map around STO (103) and LSMO (103) reflections. (c) X-ray reflectivity curve normalized to R_F and the corresponding fit for LSMO/STO film. Inset: X-ray scattering length density depth profile obtained from the best fit. (d) STEM Z-contrast image of a thinner (34 nm) LSMO/STO film sample taken down the (110) zone axis. Inset: A low magnification image. (e) Normalized, integrated EELS profiles measured along the growth direction obtained from the from the Ti $L_{2,3}$, O K, Mn $L_{2,3}$ La $M_{4,5}$ and Sr $L_{2,3}$ absorption edges. Data acquired in a Nion UltraSTEM200, operated at 200 kV, equipped with a fifth order aberration corrector and a Gatan Enfinium spectrometer.
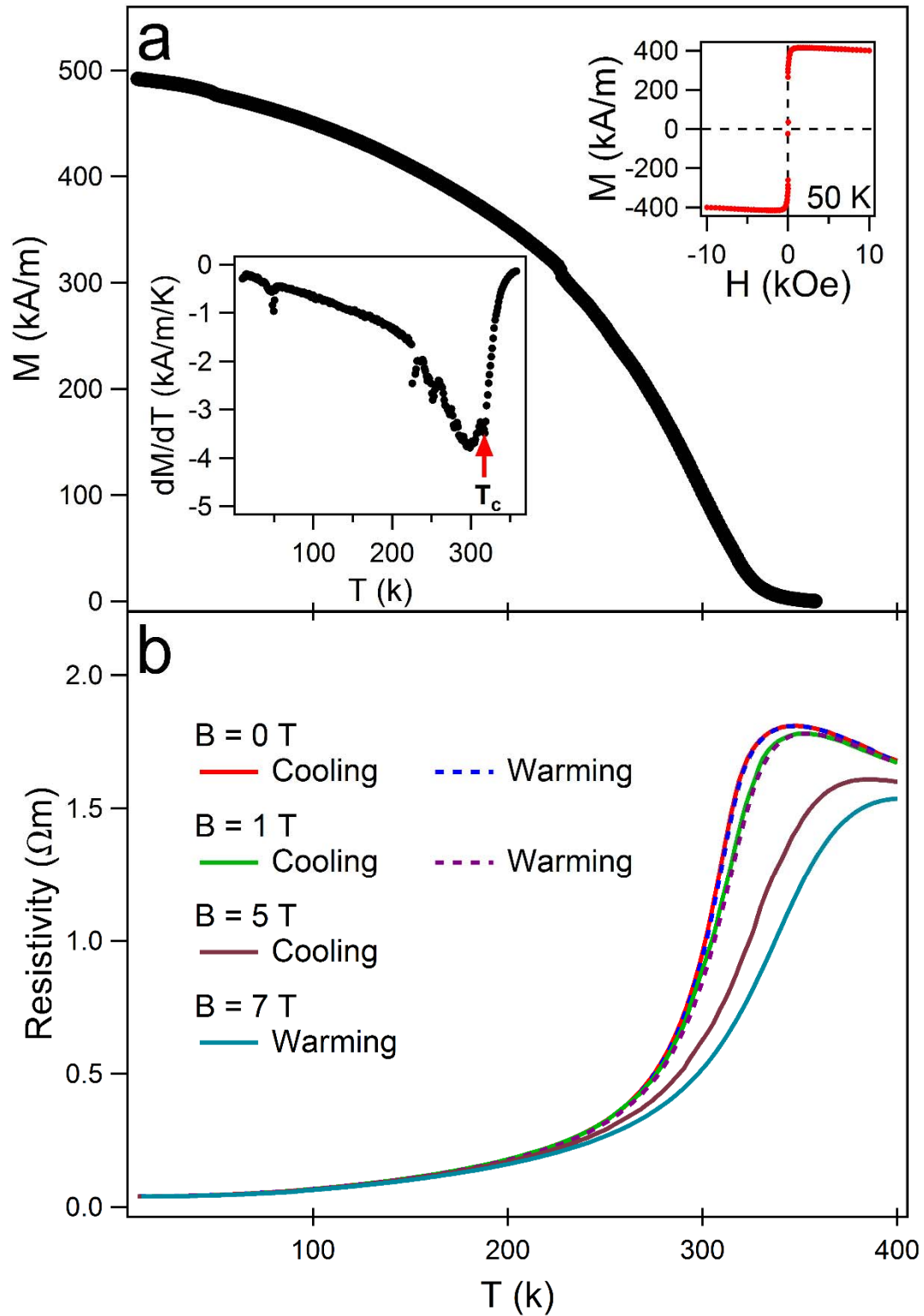
Figure 2. (a) Temperature dependence of the magnetization. Lower inset: the corresponding derivative curve. Upper inset: M-H curve at 50K and ±10 kOe. (b) Temperature dependence of the resistivity at different thermal and field conditions.
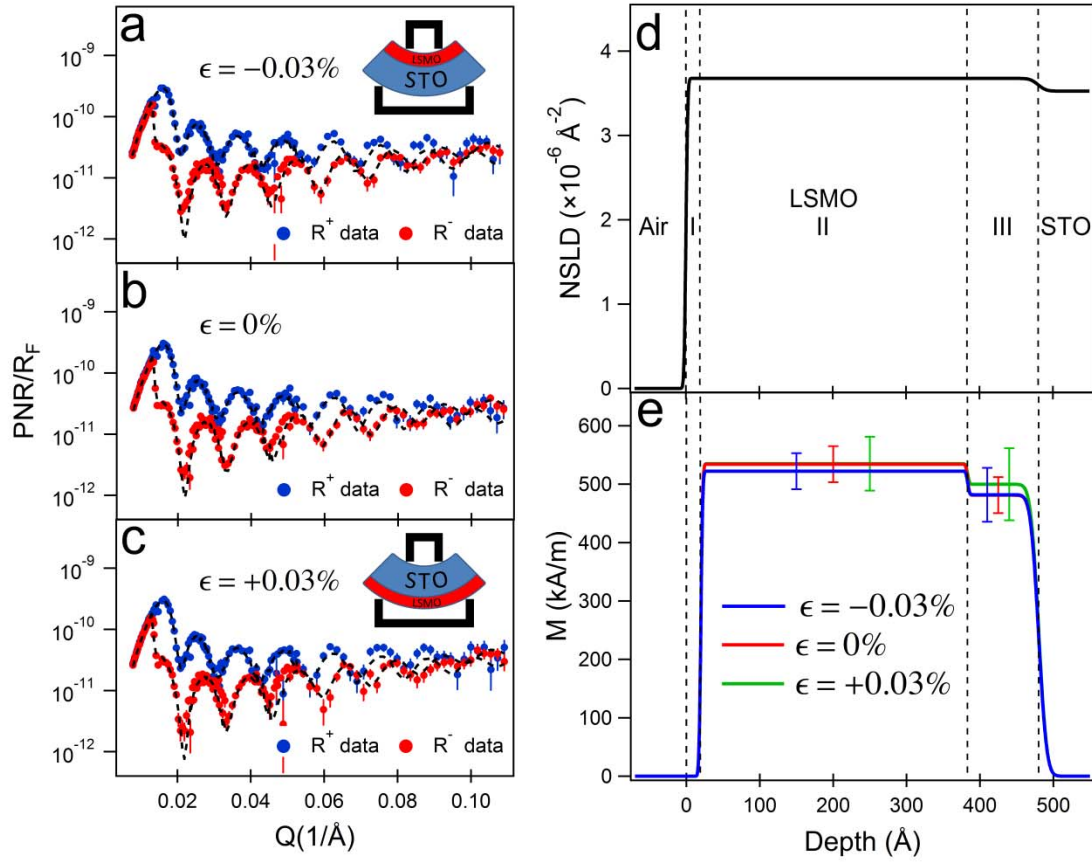
Figure 3. (a)-(c) Polarized neutron reflectivity normalized to R_F for three values of bending strain and the corresponding fits. (d) Obtained nuclear scattering length density depth profile. (e) Obtained magnetization depth profiles for three bending cases.
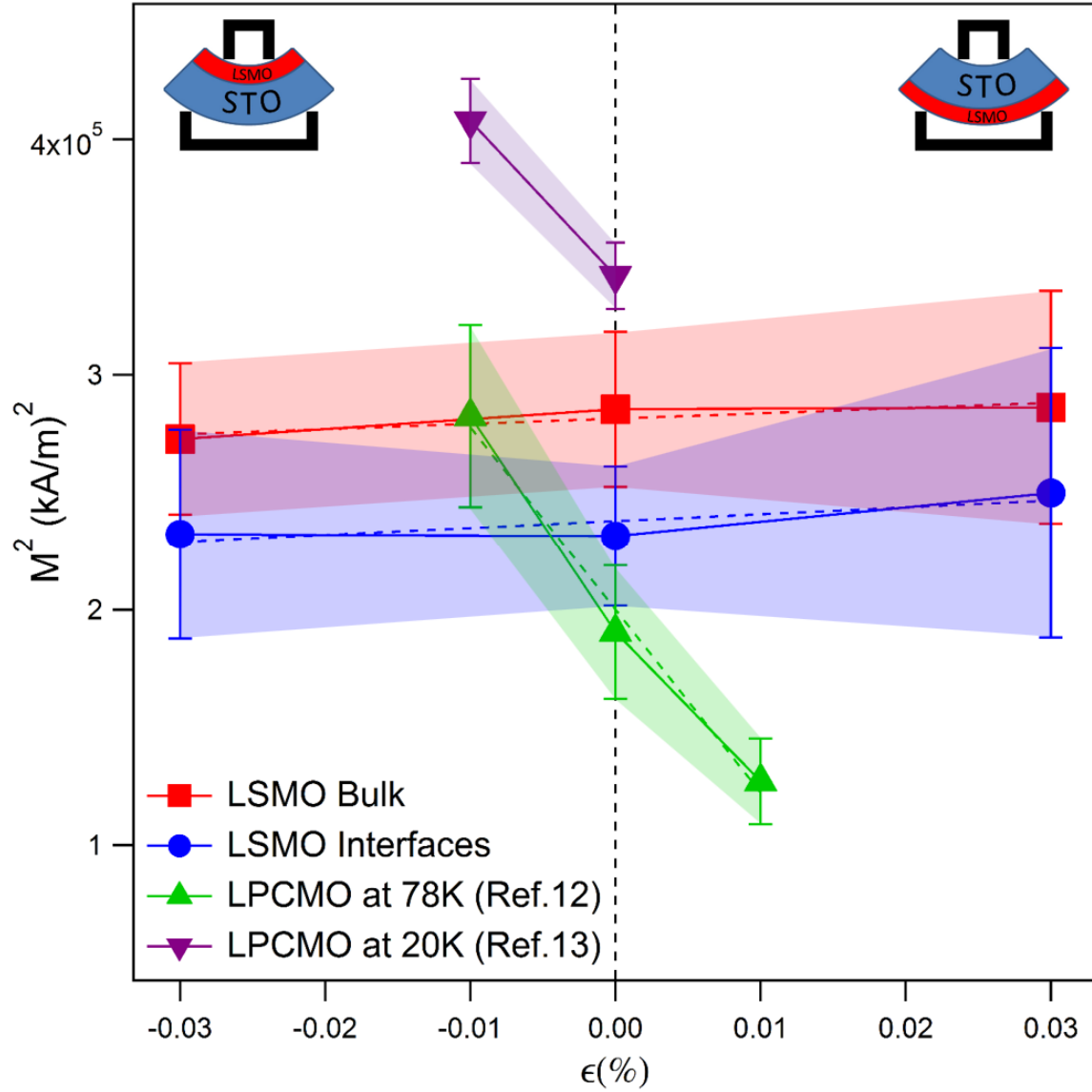
Figure 4. Square of the magnetization for the LSMO film bulk region (red), LSMO interfacial region (blue), LPCMO film bulk region at 78 K (green), and at 20 K (purple) vs. applied bending strain. The symbols represent the optimal values. The shaded regions represent the confidence of the values.

[1] W. Eerenstein, N. D. Mathur, and J. F. Scott, Nature **442**, 759–765 (2006).

[2] S. -W. Cheong, and M. Mostovoy, Nature Mater. **6**, 13 (2007).

[3] R. Ramesh, and N. A. Spaldin, Nat. Mater. **6**, 21 (2007).

[4] V. E. Wood, and A. E. Austin, Proceedings of the Symposium on Magnetoelectric Interaction Phenomena in Crystals, Seattle, 1973, edited by A. J. Freeman and H. Schmid, Gordon and Breach, New York, 181 (1975).

[5] N. A. Hill, J. Phys. Chem. B **104**, 6694 (2000).

[6] Y. Tokura, Rep. Prog. Phys. 69, 797 (2006).

[7] M. K. Lee, T. K. Nath, C. B. Eom, M. C. Smoak, and F. Tsui, Appl. Phys. Lett. **77**, 3547 (2000).

[8] C. Thiele, K. Dörr, S. Fähler, L. Schultz, D. C. Meyer, A. A. Levin, and P. Paufler, Appl. Phys. Lett. **87**, 262502 (2005).

[9] C. Thiele, K. Dörr, O. Bilani, J. Rödel, and L. Schultz, Phys. Rev. B **75**, 054408 (2007).

[10] C. A. F. Vaz, J. Hoffman, Y. Segal, J. W. Reiner, R. D. Grober, Z. Zhang, C. H. Ahn, and F. J. Walker, Phys. Rev. Lett. **104**, 127202 (2010).

[11] T. L. Meyer, A. Herklotz, V. Lauter, J. W. Freeland, J. Nichols, E.-J. Guo, S. Lee, T. Z. Ward, N. Balke, S. V. Kalinin, M. R. Fitzsimmons, and H. N. Lee, Phys. Rev. B 94, 174432 (2016).

[12] S. Singh, M. R. Fitzsimmons, T. Lookman, H. Jeen, A. Biswas, M.A. Roldan, and M. Varela, Physical Review B **85**, 214440 (2012).

[13] S. Singh, M. R. Fitzsimmons, T. Lookman, H. Jeen, and A. Biswas, Physical Review B **90**, 060407(R) (2014).

[14] A. P. Chen, *et al.*, J. Appl. Phys. **114**, 124101 (2013).

[15] P. C. Dowden, Z. Bi and Q. X. Jia, Rev. Sci. Instrum. **85**, 025111 (2014).

[16] L. G. Parratt, Phys. Rev. **95**, 359 (1954).

[17] M. R. Fitzsimmons, T. J. Silva and T. M. Crawford, Physical Review B **73**, 014420 (2006).

[18] W. H. Press, B. P. Flannery, S. A. Teukolsky, W. T. Vetterling, **Numerical Recipes, The Art of Scientific Computing** (Cambridge University Press, 1986), p. 470.

[19] M. Björck, and G. Andersson, J. Appl. Cryst. **40**, 1174 (2007).

[20] M. B. Salamon, and M. Jaime, Rev. Mod. Phys. **73**, 583(2001).

[21] M. R. Fitzsimmons, and C. Majkrzak, **Modern Techniques for Characterizing Magnetic Materials** (Springer, New York, 2005), Chap. 3, pp. 107–155.

[22] A. Misra, and M. Nastasi, **Engineering Thin Films and Nanostructures with Ion Beams** (CRC Press, 2005), Chap. 7, pp. 319.

[23] Y. T. Im, S. T. Choi, T. S. Park, and J. H. Kim, J. Mech. Sci. Tech. **18**, 12 (2004).

[24] M. Huijben, *et al*., Phys. Rev. B **78**, 094413 (2008). E. Dagotto, T. Hotta, and A. Moreo, Phys. Rep. **344**, 1–153 (2001). L. F. Kourkoutis, J. H. Song, H. Y. Hwang, and D. A. Muller, Proc. Natl. Acad. Sci. U.S.A. **107**, 11682–11685 (2010). A. Tebano, *et al*., Phys. Rev. Lett. **100**, 137401 (2008). M.B. Lepetit, B. Mercey, and C. Simon, Phys. Rev. Lett. **108**, 087202 (2012). J.–S. Lee, *et al*., Phys. Rev. Lett. **105**, 257204 (2010). M. Huijben, *et al*., Adv. Mater. Interfaces **2**, 1400416 (2015).

[25] E. Guo, T. Charlton, H. Ambaye, R. D. Desautels, H. N. Lee, and M. R. Fitzsimmons, ACS Appl. Mater. Interfaces **9**, 19307 (2017).

[26] A. J. Millis, T. Darling, and A. Migliori, J. Appl. Phys. **83**, 1588 (1998).

[27] K. H. Ahn, T. Lookman, and A. R. Bishop, Nature **428,** 401 (2004).

[28] W. Wu, C. Israel, N. Hur, S. Park, S.-W. Cheong, and A. de Lozanne, Nature Materials **5**, 881 (2006).

[29] T. Dhakal, J. Tosado, and A. Biswas, Phys. Rev. B **75**, 092404 (2007).

[30] F. A. McClintock, and A. S. Argon, **Mechanical Behavior of Materials** (Addison-Wesley Publishing Co., 1966), p. 349.

[31] I. C. Infante, F. Sánchez, J. Fontcuberta, M. Wojcik, E. Jedryka, S. Estradé, F. Peiró, J. Arbiol, V. Laukhin, and J. P. Espinós, Phys. Rev. B **76**, 224415 (2007).

[32] P. Gumbsch, S. Taeri-Baghbadrani, D. Brunner, W. Sigle, and M. Ruhle, Phys. Rev. Lett. **87**, 085505 (2001).